APL Materials

Trade-off between variability and retention of memristive epitaxial $SrTiO_3$ devices

Cite as: APL Mater. **9**, 021110 (2021); https://doi.org/10.1063/5.0035707
Submitted: 30 October 2020 . Accepted: 04 January 2021 . Published Online: 05 February 2021

Jan L. Rieck, Felix V. E. Hensling, and Regina Dittmann

Trade-off between variability and retention of memristive epitaxial $SrTiO_3$ devices

Cite as: APL Mater. 9, 021110 (2021); doi: 10.1063/5.0035707
Submitted: 30 October 2020 • Accepted: 4 January 2021 •
Published Online: 5 February 2021

Jan L. Rieck,[a] Felix V. E. Hensling, and Regina Dittmann[a]

AFFILIATIONS

Peter Gruenberg Institute 7, Forschungszentrum Juelich GmbH, 52425 Juelich, Germany and JARA-FIT, RWTH Aachen University, 52056 Aachen, Germany

[a]Authors to whom correspondence should be addressed: jan.rieck@rwth-aachen.de and r.dittmann@fz-juelich.de

ABSTRACT

We present a study of the trade-off between the retention and variability of $SrTiO_3$-based memristive devices. We identified the applied switching current and the device stoichiometry as main influence factors. We show that the SrO formation at the electrode interface, which has been revealed to improve the device retention significantly, is associated with an increased cycle-to-cycle and device-to-device variability. On the other hand, devices with homogeneous, Ti-terminated $SrTiO_3$–Pt interfaces exhibit poor retention but the smallest variability. These results give valuable insights for the application of memristive $SrTiO_3$ devices as non-volatile memory or in neural networks, where the control of variability is of key relevance.

One of the most promising candidates for future-non-volatile memories and neuromorphic applications is the resistive random access memory (ReRAM).[1–5] These memories can be realized by a broad variety of materials. Besides established transition metal oxides, biomaterial-based or hexagonal boron nitride memristors were shown to exhibit synaptic functions such as short-term or long-term plasticity, allowing their implementation as artificial synapses used in large-scale deep neural networks.[6,7] Generally, these memories are based on a reversible change in the electrical resistance upon applying an electrical bias to an active layer sandwiched between two electrodes. This process is commonly referred to as "resistive switching" or "memristive phenomenon." By switching between a low resistive state (LRS) and a high resistive state (HRS), the device resistance can be encoded in the logical states ON and OFF.[8] $SrTiO_3$ is a well-researched transition metal oxide exhibiting filamentary resistive switching.[9–11] The epitaxial single crystal $SrTiO_3$ devices of this work exhibit filamentary switching in the so-called eight-wise sense, meaning that the LRS is set by a positive bias applied to the Schottky-type interface. We have shown in our previous work that this can be explained by reversible release and reincorporation of oxygen in the filament. The oxygen is stored in or beneath the Pt top electrode or supplied by the atmosphere.[12,13] It was reported that the choice of the stacking layer sequence and, thus, the top electrode-oxide interface as well as the atmospheric humidity strongly influence the switching mechanism.[14] We have previously studied how the retention of $SrTiO_3$-based devices can be improved by growth induced structural changes. Stoichiometric devices with homogeneous, Ti-terminated $SrTiO_3$–Pt interfaces exhibit poor retention, whereas, however, promoting the SrO island formation at the $SrTiO_3$–Pt interface results in an improved retention. This can be attributed to SrO islands acting as an oxygen diffusion barrier and, thus, preventing the reoxidation of the conducting filament by ambient oxygen.[10,15] Different strategies are available to realize the formation of SrO on top of $SrTiO_3$: (i) the segregation of SrO islands to the surface as an accommodation mechanism for Sr-rich growth,[16,17] (ii) directly depositing a few unit cells of SrO on stoichiometric $SrTiO_3$ thin films,[18] or (iii) applying an increased forming or switching current compliance that promotes the SrO segregation through the corresponding enhanced Joule heating.[10,15,19] Recently, another work demonstrated the tuning of retention in the timeframe of minutes of $SrTiO_3$-based devices by engineering the electrode/oxide interface through controlling the Al content in the Pt top electrode.[20] Apart from interface effects, Ruddlesden–Popper-type antiphase boundaries (APBs), which occur as an additional accommodation mechanism for Sr-rich growth, act as preformed filaments.[21] By artificially engineering these APBs, we fabricated forming-free memristive devices.[21] All these previous studies have focused on the improvement of the retention and on understanding

the underlying mechanisms; however, they all lack considering how the applied changes influence the variability.

One of the major challenges in establishing memristive devices for non-volatile memory is their large cycle-to-cycle (C2C) and device-to-device (D2D) variability in both the HRS and LRS. However, the inherent variability of the devices can be utilized for the emerging field of neuromorphic computing to introduce stochasticity and thereby improve learning efficiency or demonstrate the robustness of a neural network.[22–24] To take advantage of the variability of $SrTiO_3$ memristive devices, it is crucial to understand the underlying mechanism and eventually to control it. In our previous work, we have unraveled the basic mechanisms behind the C2C and D2D variability of $SrTiO_3$ memristive devices.[25] We showed that the stochastic nature of the conducting filament leads to different filament shapes or variations of its oxygen vacancy distribution. During forming and switching, a competitive growth of multiple prefilaments, rather than one main conducting filament, prevails. Since this process severely differs for each device, D2D variability is observed. Variations in the active filament position between different switching cycles have been found to cause C2C variability.[25] In this article, we will present detailed studies of the D2D and C2C variability in $SrTiO_3$ memristive devices in dependence of the processing and electroforming conditions. We achieve this by considering the influence of well-known main factors on the performance of $SrTiO_3$ memristive devices, namely, the stoichiometry of the epitaxial $SrTiO_3$ films,[16,18,21] the deposition of additional SrO at the top electrode interface,[18] and the current compliance applied during the forming step.[10,15,19] The aforementioned influence factors result in two structural features, namely, SrO islands and Ruddlesden–Popper-type APBs. These features have been shown to significantly improve the device retention.[18] Therefore, we focus on SrO islands rather than a homogeneous oxygen diffusion barrier to investigate if they influence the variability as well. This work points out that the variability is increased, resulting in a trade-off between retention and variability.

A sketch of our memristive device geometry is shown in Fig. 1(a). The active layers of the memristive devices are 20 nm thick epitaxial $SrTiO_3$ thin films deposited by pulsed laser deposition (PLD) on TiO_2-terminated 0.5 wt. % Nb-doped $SrTiO_3$ substrates, which simultaneously function as a conducting bottom electrode. The substrate temperature during deposition was set to 800 °C by an infrared laser. The heating rate was 50 °C/min, while a cooldown to below 250 °C was achieved approximately in 30 s. The oxygen pressure was 0.1 mbar. The $SrTiO_3$ target is ablated by a KrF excimer laser emitting ultraviolet light with a wavelength of 248 nm at a pulse rate of 5 Hz and a spot size of 2 mm^2, while the target-to-substrate distance was set to 44 mm. In order to grow $SrTiO_3$ films of varying stoichiometry, the laser fluence was varied, as introduced in previous publications.[16,17,26,27] For stoichiometric and Sr-rich $SrTiO_3$ films, laser fluences of 1.05 J/cm^2 and 0.67 J/cm^2 were used, respectively. For one sample, additional SrO (green) on top of the stoichiometric $SrTiO_3$ was ablated from a ceramic strontium peroxide (SrO_2) target with a laser frequency of 1 Hz at a laser fluence of 1.21 J/cm^2 and an oxygen pressure of 2×10^{-7} mbar with a nominal thickness of 3 unit cells subsequently to the $SrTiO_3$ deposition. As the top electrode, a 10 nm Pt layer (light gray) was evaporated. The Pt layer was patterned using photolithography and Ar ion beam etching, resulting in 19×16 μm^2 electrodes. The 70 nm layer of HfO_2 (dark blue) deposited by sputtering has an overlap of a few micrometer at the Pt top electrode edge to prohibit switching events outside the electrode boundaries. As electrical leads to the Pt top electrode, contact pads were evaporated, consisting of 10 nm Pt and 110 nm Au films

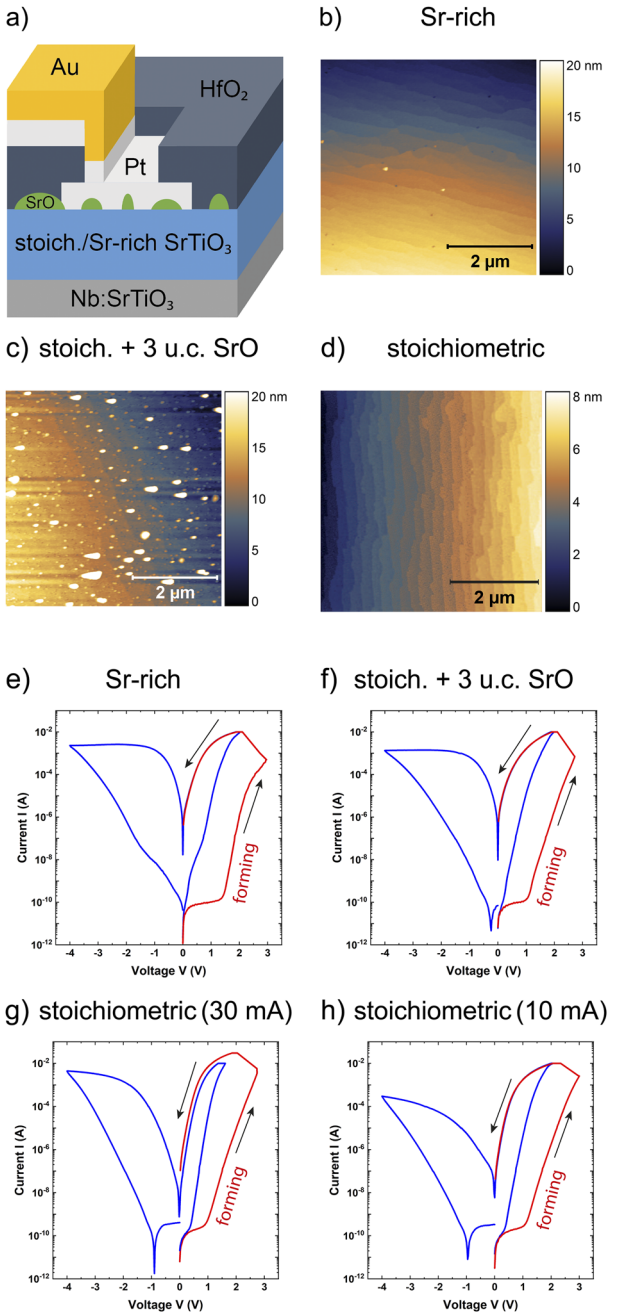

FIG. 1. (a) General device design. The topography of (b) Sr-rich $SrTiO_3$, (c) stoichiometric $SrTiO_3$ with a 3 unit cell thick layer of SrO, and (d) stoichiometric $SrTiO_3$. The IV-curve for (e) Sr-rich $SrTiO_3$, (f) stoichiometric $SrTiO_3$ with a 3 unit cell thick layer of SrO, and stoichiometric $SrTiO_3$ with (g) 30 mA and (h) 10 mA forming current compliance. In each IV-curve, the forming sweep is shown in red.

(yellow). These contact pads are crucial for electrical characterization since directly contacting the Pt top electrode with W whisker probes causes a strong variability due to the varying contact resistance. A bias is applied to the Pt top electrode, while the Nb:$SrTiO_3$ bottom electrode is electrically grounded. To investigate the influence of the current compliance during forming, the forming step for stoichiometric devices was limited by a current compliance of 10 mA and 30 mA, respectively. All subsequent SETs were limited by a current compliance of 10 mA. The latter was also used for the forming and all SETs of the other samples in this work.

Generally, the variability of memristive devices can be changed by all details of fabrication. We have shown in earlier studies that the switching mechanism can potentially change with the film thickness from eightwise to counter-eightwise.[28] To exclude this additional influence factor, we exclusively investigated devices of 20 nm $SrTiO_3$ thickness. Since the scope of this work is the retention-variability trade-off, we did not vary the device size as no influence of device size on the retention was found in previous works.

The $SrTiO_3$ film topographies were analyzed right after deposition using an Oxford Instruments Asylum Research Cypher atomic force microscope (AFM). In Fig. 1(b), the topography of the Sr-rich film with scattered SrO precipitates with a varying diameter of 20 nm–150 nm is shown. The black features are etch pits resulting from substrate preparation.[29,30] In comparison to that, the topography of a stoichiometric film with 3 unit cell SrO on top exhibits a much larger SrO island density and SrO island diameters of 200 nm–500 nm, as shown in Fig. 1(c). Due to the 3D growth mode transition of SrO on $SrTiO_3$, SrO islands of varying thicknesses are formed instead of a homogeneous layer.[18] The topography of a stoichiometric $SrTiO_3$ thin film without any SrO precipitates is shown in Fig. 1(d).

The bottom half of Fig. 1 shows the IV-curves of the forming and the subsequent sweep for one exemplary device of all four samples. Figure 1(e) shows a Sr-rich device, while the IV-curve for a stoichiometric device with additional SrO on top is shown in Fig. 1(f). The IV-curves for stoichiometric devices formed with 30 mA and 10 mA are depicted in Figs. 1(g) and 1(h), respectively. All samples show distinct forming steps. In Fig. 1(g), the increased forming current compliance of 30 mA is noticeable by the higher maximum of the forming sweep. Differences in the LRS resistance of the samples can be estimated by comparing the currents at the left branch of the sweep. The current at the right branch is limited by the current compliance, which is mostly reached at a voltage of less than 2 V. Thus, sample differences are masked at this branch. Compared to the stoichiometric device formed at 10 mA, all other devices show higher currents at the left branch, indicating a lower LRS resistance. The generally lower LRS resistance for Sr-rich devices and stoichiometric devices with additional SrO is in accordance with our previous work.[18] The lowering of LRS resistance for stoichiometric devices by a pronounced forming step with 30 mA current compliance was revealed in Ref. 10. We attribute it to a higher power dissipation and thereby increased mobility of the oxygen vacancies during forming with higher currents.

To investigate the C2C variability, the device is SET and RESET by a rectangular pulse sequence, which is repeated over 2000 cycles. After each SET and RESET, respectively, the LRS and HRS resistance is measured by a readout pulse of +0.5 V. To analyze the D2D variability, this measurement procedure is repeated for 10 different pristine devices of the same sample. Devices, which were defective due to lithography faults, are excluded, and a device yield is given for every sample representing the ratio of usable devices. The measured LRS and HRS resistances of the device sets are shown in Fig. 2 in individual Weibull plots for each sample. The gray

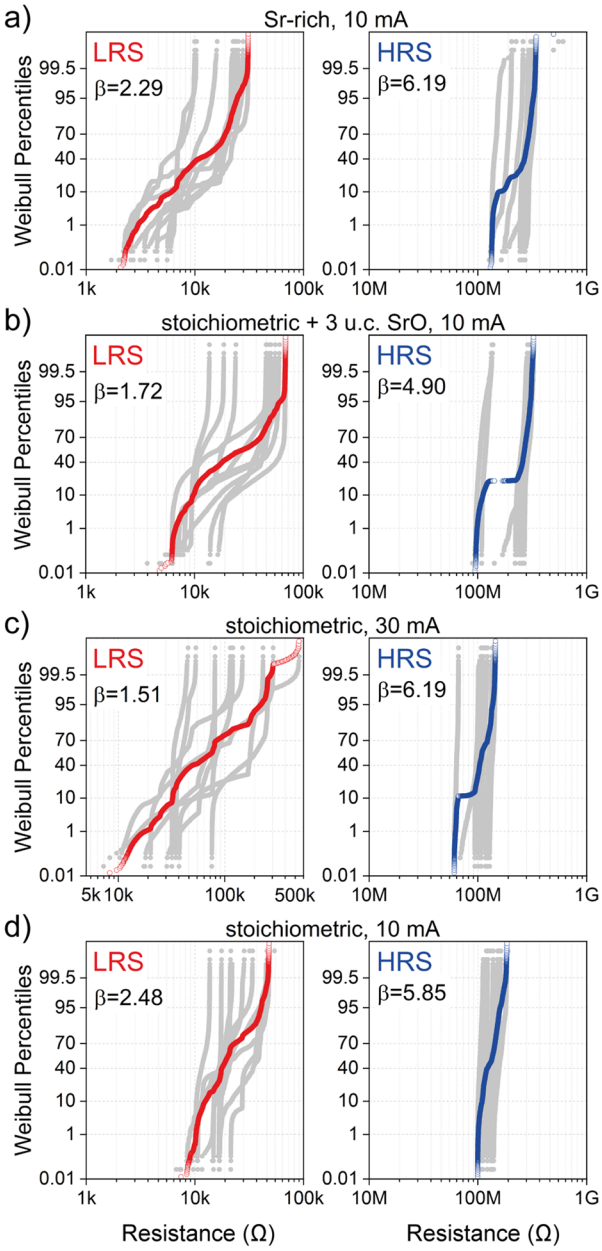

FIG. 2. Weibull plots for the LRS and HRS. Gray graphs show individual devices, while the colored graphs show the corresponding accumulated data. For each colored graph, the Weibull slope β is given. Data shown of devices with (a) Sr-rich $SrTiO_3$ and (b) stoichiometric $SrTiO_3$ with additional SrO on top. For devices with stoichiometric $SrTiO_3$, (c) a 30 mA (only 9 devices) and (d) a 10 mA forming current compliance were investigated. Note the adjusted resistance scale in the LRS of (c). Except for (c), the forming current compliance was 10 mA. Switching current compliance was always 10 mA.

graphs in the background represent data of the individual usable devices and depict the C2C variability of the samples. The colored graphs represent the accumulated variability of the respective samples, which is dominated by the D2D variability. To give a quantitative value for the D2D variability of the LRS and HRS of each sample, each colored graph of accumulated data is fitted by a Weibull distribution, respectively. In this double-logarithmic depiction, the Weibull distribution and all data, which can be well described by it, will show a linear behavior.[31] Therefore, one can imagine the Weibull distribution fit as a straight line describing each colored graph. For the sake of clarity, the fit is not shown in Fig. 2. However, the slope of the fit, called the Weibull slope β, is extracted. For 10 devices with almost identical resistance values, the accumulated graph is rather described by a steep line of large slope spreading over a small resistance interval. Therefore, low D2D variability is indicated by large values of β. On the other hand, 10 devices behaving vastly different from each other result in an accumulated graph that spreads over a large resistance range. This graph can be best fitted with a rather flat line of small slope. Accordingly, high D2D variability is indicated by a small value of β. The inset of each individual Weibull plot shows the value of β for the accumulated graph.

Considering all Weibull plots in Fig. 2, one observation is immediately apparent. The HRS exhibits sample independent almost no C2C variability. We will, thus, in the following only discuss the D2D variability of the HRS as well as both the C2C and D2D variability of the LRS.

Figure 2(a) shows the Weibull plot of Sr-rich devices switched with the usual 10 mA forming step current compliance. The device yield is 67%. The HRS resistance values lie between 130 MΩ and 340 MΩ. Regarding the gray graphs for individual devices, two devices show a slightly lower resistance than the majority. The Weibull slope of the HRS is β = 6.19. In comparison to that, the LRS resistance values are more scattered, reaching from 2 kΩ to 30 kΩ. As for the HRS, three individual devices show lower resistance than the device majority. The Weibull slope of β = 2.29 for the LRS points out a higher D2D variability compared to the HRS. Furthermore, the gray graphs for individual devices in the LRS exhibit resistance fluctuations, revealing an increased C2C variability for Sr-rich $SrTiO_3$.

In Fig. 2(b), the Weibull plots of stoichiometric $SrTiO_3$ devices with SrO islands deposited on top of stoichiometric $SrTiO_3$ are shown. The device yield is 85%. The HRS resistance values range from 100 MΩ to 320 MΩ, indicating a bimodal resistance split-up with two groups of, respectively, two and eight devices of different resistances. Due to the resistance split, the HRS shows the lowest β = 4.90 among all investigated samples and, therefore, the highest D2D variability. However, within each group, β is markedly lower. While the 2-device group of lower HRS exhibits β = 14.45, β = 14.09 for the 8-device group of higher HRS. Looking at the LRS of Fig. 2(b), a similar resistance split is revealed. Within the LRS resistance range of 5 kΩ–70 kΩ, three devices exhibit a markedly lower resistance than most devices. However, these devices are not the same as the ones from the 2-device group in the HRS. Due to the resistance split, the LRS Weibull slope of β = 1.72 is significantly lower than β of the Sr-rich devices, thus indicating a higher D2D variability. It is important to note that the impact on the C2C variability is vice versa. The gray graphs in the LRS appear slightly smoother compared to the Sr-rich devices, thus indicating a lower C2C variability. Hence, depositing additional SrO on top of stoichiometric $SrTiO_3$ increases the D2D variability, both in the LRS and HRS, but decreases the C2C variability.

Figure 2(c) shows the Weibull plot of stoichiometric devices for an increased forming current compliance of 30 mA with a device yield of 82%. The HRS resistances range from 60 MΩ to 145 MΩ. One device shows a marked lower resistance than the device majority. The D2D variability in the HRS is comparable with the Sr-rich devices as the Weibull slope β = 6.19 is equal. However, the LRS resistance values of 30 mA formed devices cover almost two orders of magnitude from 8 kΩ to 500 kΩ. This results both in the highest average LRS resistance and the highest LRS D2D variability of all samples as indicated by the small Weibull slope of β = 1.51. The gray graphs indicate a slightly higher C2C variability as that of stoichiometric devices with additional SrO.

In Fig. 2(d), the Weibull plot of stoichiometric devices formed with a 10 mA current compliance is depicted. The device yield is 83%. The HRS resistance values lie between 100 MΩ and 185 MΩ, leading to an intermediate Weibull slope of β = 5.85 compared to the other samples. The uniform distribution of the HRS resistance values for all devices is remarkable. Furthermore, the average HRS resistance for stoichiometric devices is lower compared to that of Sr-rich devices formed at the same current compliance. Regarding the LRS, the resistance values range from 8 kΩ to 50 kΩ. The LRS shows two groups of devices, one group of six devices with largely scattered, lower resistances and one group with four devices of higher and narrowly distributed resistances. However, the comparably small resistance range results in a high β = 2.48. This indicates a slightly lower D2D variability in the LRS for stoichiometric devices formed at 10 mA current compliance compared to the Sr-rich reference and all other samples. The C2C variability of stoichiometric devices formed at 10 mA is the lowest among all samples.

In short, compared to the LRS of the Sr-rich devices as a reference, a lower C2C variability is found for stoichiometric devices formed at 10 mA current compliance. However, the comparably low LRS D2D variability of Sr-rich devices can only be outperformed by stoichiometric devices formed at 10 mA current compliance without additional SrO. The investigated samples suggest that the retention-improving factors go along with an increase in the variability. Below, we will discuss the underlying mechanisms of this observation.

For Sr-rich $SrTiO_3$ devices, an increased C2C variability was found. As sketched in Fig. 3(a), we assign this to the presence of preformed filaments and the formation of SrO islands on top of it. The preformed filaments emerge at the location of extended defects, more precisely Ruddlesden–Popper-type APBs,[21] which were shown to locally pinpoint native oxygen vacancies in SrTiO3.[32–34] We have further shown that the formation of SrO islands results from the occurrence of Ruddlesden–Popper-type APBs underneath since the Sr ion migration energy along these is significantly lower.[35] The SrO islands on the top of Sr-rich films are depicted in the topography of Fig. 1(b). In Fig. 3(a-I), both the preformed filaments and the SrO islands of Sr-rich films are depicted. During forming, a conducting filament will emerge at the location of a preformed filament, as shown in Fig. 3(a-II). We expect that further SrO precipitates emerge in Sr-rich $SrTiO_3$ devices during forming and repeated setting at the given current compliance.[35] Therefore, pronounced SrO segregation above the conducting filaments takes place after the forming step as depicted by the enhanced size of the SrO island in Fig. 3(a-II).

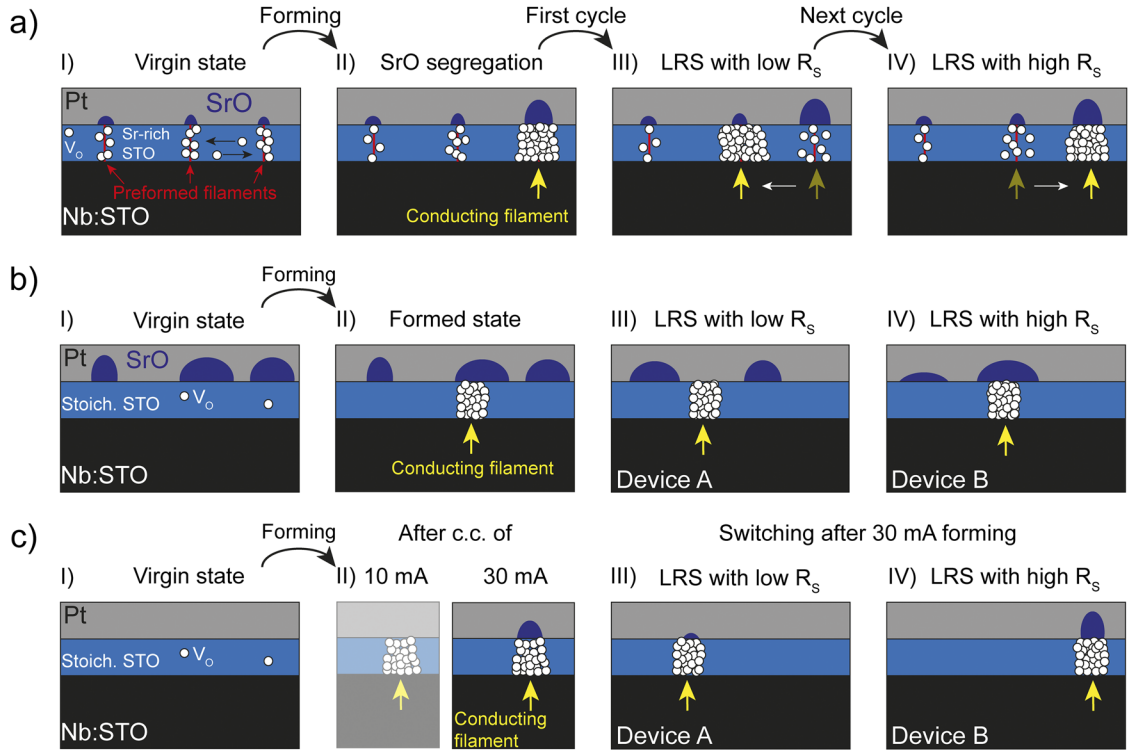

FIG. 3. Illustrations of possible underlying mechanisms for (a) increased C2C variability for Sr-rich $SrTiO_3$ devices, (b) increased D2D variability for devices of stoichiometric $SrTiO_3$ with additional SrO on top, and (c) increased D2D variability for stoichiometric $SrTiO_3$ devices with a more pronounced forming current compliance of 30 mA.

Since the segregation occurs in a non-homogeneous way, the SrO islands exhibit varying sizes. As SrO has a higher bandgap than $SrTiO_3$,[36,37] the SrO islands will act as an additional serial resistance for the current flowing through the filament underneath. If a small SrO island is located above the conducting filament, the resulting LRS resistance is rather low, as depicted in Fig. 3(a-III). Due to the high density of preformed filaments in the vicinity, a lateral filament shift to another position is facilitated. Thus, in the next cycle, the filament has changed to the location of a former preformed filament with a pronounced SrO precipitate above, as shown in Fig. 3(a-IV). Due to the enhanced size of the SrO island compared to the previous cycle and, thus, higher serial resistance, this LRS exhibits a higher resistance in total. This mechanism can explain the increased C2C variability for Sr-rich $SrTiO_3$ films. Furthermore, the high density of preformed filaments enhances the shift between different filament positions during switching. Therefore, it seems natural that C2C variability can be reduced by controlling the active filament position as demonstrated in other works.[38–40]

For stoichiometric $SrTiO_3$ with additional SrO deposited on top, a decreased C2C and increased D2D variability as well as a bilateral resistance split for both LRS and HRS was observed. The decreased C2C variability can be explained by the absence of preformed filaments underneath the SrO islands compared to the scenario for Sr-rich thin films, as seen in Fig. 3(a). However, both the increased D2D variability and the resistance split can be assigned to the pronounced SrO islands at the top interface, as depicted in Fig. 3(b). As shown in the topography of Fig. 1(c), the SrO islands are densely scattered and measure 150 nm to almost 300 nm in diameter. The height of the largest islands even reaches up to 50 nm. In Fig. 3(b), this is illustrated by large SrO clusters. The fact if the filament is covered by an SrO island or not defines the resistance of the LRS. Therefore, the device will exhibit a low resistance if the filament is located between SrO islands, as depicted in Fig. 3(b-III). The analog case for a high resistance LRS is shown in Fig. 3(b-IV), when the filament is located below a large SrO precipitate. The low (high) resistive branches in the LRS of Fig. 2(b) correspond to the illustrated cases in Figs. 3(b-III) and 3(b-IV). This mechanism explains not only the occurrence of the bimodal resistance split in the LRS but also the high D2D variability. However, the devices of the low resistive branch in the LRS of Fig. 2(b) are different from the devices of the low resistive branch in the HRS. Therefore, the resistance split in the HRS cannot be fully explained up to this point.

For the stoichiometric $SrTiO_3$ sample formed with a higher current compliance of 30 mA, an increased D2D variability was detected. The current limit increase from 10 mA to 30 mA for the forming step is accompanied by enhanced Joule heating in the device. Hence, an increased current compliance will markedly boost the thermal power due to its quadratic correlation. As the forming and switching process is restricted to a single or a few low diameter conducting filaments,[41,42] this confinement results in an extremely high heat dissipation and, thus, correspondingly high temperatures.[43] Joule heating acts as the major driving process

TABLE I. Overview of sample parameters indicating a trade-off between variability and retention. The Weibull slope β indicating the D2D variability as well as the results for C2C variability refers to the LRS, respectively, based on Fig. 2. The retention results are based on our previous works.[10,18]

$SrTiO_3$	SrO island occurrence	β (D2D var.)	C2C var.	R_{OFF}/R_{ON} after 300 h (retention)
Sr-rich	Intermediate	2.29 (higher)	Highest	1000
Stoich. + 3 u.c. SrO	Large	1.72 (higher)	Higher	10 000
Stoich. (30 mA)	After forming	1.51 (highest)	Higher	10
Stoich. (10 mA)	None	2.48 (lowest)	Lowest	1

behind a SrO phase separation in the thin film during forming and switching.[19] Therefore, the increased current compliance results in an enhanced SrO segregation at the interface above the filament's position. This is depicted in Figs. 3(c-I) and 3(c-III). Due to the irreversible segregation of SrO islands, the forming step will also affect all subsequent switching cycles. Since the amount of segregated SrO generally fluctuates, the serial resistance of the respective SrO island will vary as well. If the SrO islands of one device tend to be comparably small, the LRS of this device will exhibit a lower total resistance, as depicted in Fig. 3(c-III). On the other hand, a comparably large precipitate in another device will lead to a high-Ohmic LRS, as seen in Fig. 3(c-IV). Overall, the LRS resistance of devices formed with 30 mA current compliance will always be higher than for devices formed with 10 mA current compliance, as seen in Figs. 2(c) and 2(d). Since a 10 mA current compliance forming does not result in SrO precipitates, these devices lack an additional serial resistance.[15] Hence, we can explain the increase in D2D variability in the LRS with a higher forming current compliance by the enhanced SrO expulsion, resulting in varying additional serial resistances. As a result of that, one can conclude that a weaker forming or no forming at all can result in lower variability. This observation is in accordance with Ref. 44, in which a low variability was found for forming-free ReRAM devices as electroforming is typically of stochastic nature and leads to a hardly controllable filament formation. The increased C2C variability in the LRS for a more pronounced forming step, as seen in Fig. 2(c), remains subject to further research. However, a possible explanation could be the formation of a subfilamentary network[45,46] upon forming, which facilitates the lateral filament movement underneath the SrO islands of varying sizes.

Considering all above-described mechanisms, we find two main influence factors on the variability. The occurrence of SrO islands is generally accompanied by an increase in D2D variability. We ascribe this to the variation of size, location, and density of these islands, in turn resulting in variable additional serial resistances. Devices with Ruddlesden–Popper-type APBs are expected to show an increased C2C variability. As Ruddlesden–Popper-type APBs act as preformed filaments in $SrTiO_3$ devices,[21] a sufficient density of these preformed filaments can be expected to promote movement between the filament positions, thus explaining an increased C2C variability.

Table I shows an overview of the investigated samples including their SrO island occurrence and the Weibull slope β based on Fig. 2 indicating the D2D variability and C2C variability classification. All samples with SrO island occurrence exhibit an increased D2D variability. The highest D2D variability is found for stoichiometric $SrTiO_3$ formed with 30 mA as the SrO islands occur exactly at the filament's location for this sample. An increased C2C variability is found for all samples except stoichiometric $SrTiO_3$ formed with 10 mA. Sr-rich $SrTiO_3$ exhibits the highest C2C variability as described before. The rightmost column shows, based on our previous works, the memory window in the form of the ratio between R_{OFF} and R_{ON} of the devices 300 h after the SET process, indicating the retention.[10,18] The memory window of 1 for the stoichiometric device formed at 10 mA in the bottom row of Table I indicates that the HRS and LRS are no longer distinguishable. One should note that the retention results for "*stoich* (30 mA)" refer to devices formed and switched with a 30 mA current compliance,[10] while the 30 mA data of this work refer to 30 mA forming but 10 mA switching. However, Ref. 10 also showed that forming and switching with a 30 mA current compliance improves the device retention over 300 h compared to a 10 mA current compliance. Table I clarifies the trade-off between retention and variability for all samples. While all samples with retention-improving SrO islands exhibit increased C2C and D2D variability, low variability is only found for samples that exhibit an inferior retention such as stoichiometric $SrTiO_3$ devices with 10 mA forming.

In this work, we have investigated the impact of key influence parameters on the performance of $SrTiO_3$ memristive devices on their C2C and D2D variability, especially in the LRS. We considered the stoichiometry, the intentional deposition of SrO at the top interface, and the forming current compliance. All these findings point out a trade-off between device retention and variability. They could be applied to similar material systems, in which the retention is stabilized by inhomogeneous structures above the filament. Future investigations should be carried out to investigate the impact of homogeneous retention stabilizing structures such as additional oxide layers.

We acknowledge funding from the W2/W3 program of the Helmholtz Association. This research was supported by the Deutsche Forschungsgemeinschaft (Grant No. SFB 917 "Nanoswitches"), the Helmholtz Association Initiative and Networking Fund under Project No. SO-092 (Advanced Computing Architectures, ACA), and the Federal Ministry of Education and Research (Project NEUROTEC, Grant No. 16ES1133K).

DATA AVAILABILITY

The data that support the findings of this study are available from the corresponding author upon reasonable request.

REFERENCES

[1] A. Sawa, Mater. Today **11**, 28 (2008).
[2] R. Waser and M. Aono, *Nanoscience and Technology A Collection of Reviews from Nature Journals* (Nature Materials, 2009), p. 158.
[3] J. J. Yang, M. D. Pickett, X. Li, D. A. A. Ohlberg, D. R. Stewart, and R. S. Williams, Nat. Nanotechnol. **3**, 429 (2008).
[4] H.-S. P. Wong, H.-Y. Lee, S. Yu, Y.-S. Chen, Y. Wu, P.-S. Chen, B. Lee, F. T. Chen, and M.-J. Tsai, Proc. IEEE **100**, 1951 (2012).
[5] H. Abbas, Y. Abbas, G. Hassan, A. S. Sokolov, Y.-R. Jeon, B. Ku, C. J. Kang, and C. Choi, Nanoscale **12**, 14120 (2020).
[6] J. Ge, D. Li, C. Huang, X. Zhao, J. Qin, H. Liu, W. Ye, W. Xu, Z. Liu, and S. Pan, Nanoscale **12**, 720 (2020).
[7] G. Dastgeer, H. Abbas, D. Y. Kim, J. Eom, and C. Choi, Phys. Status Solidi RRL **15**, 2000473 (2020).
[8] D. B. Strukov, G. S. Snider, D. R. Stewart, and R. S. Williams, Nature **453**, 80 (2008).
[9] C. Baeumer, C. Schmitz, A. Marchewka, D. N. Mueller, R. Valenta, J. Hackl, N. Raab, S. P. Rogers, M. I. Khan, S. Nemsak, M. Shim, S. Menzel, C. M. Schneider, R. Waser, and R. Dittmann, Nat. Commun. **7**, 12398 (2016).
[10] N. Raab, C. Bäumer, and R. Dittmann, AIP Adv. **5**, 047150 (2015).
[11] R. Waser, J. Nanosci. Nanotechnol. **12**, 7628 (2012).
[12] T. Heisig, C. Baeumer, U. N. Gries, M. P. Mueller, C. La Torre, M. Luebben, N. Raab, H. Du, S. Menzel, D. N. Mueller, C.-L. L. Jia, J. Mayer, R. Waser, I. Valov, R. A. De Souza, R. Dittmann, C. La Torre, M. Luebben, N. Raab, H. Du, S. Menzel, D. N. Mueller, C.-L. L. Jia, J. Mayer, R. Waser, I. Valov, R. A. De Souza, and R. Dittmann, Adv. Mater. **30**, 1800957 (2018).
[13] D. Cooper, C. Baeumer, N. Bernier, A. Marchewka, C. La Torre, R. E. Dunin-Borkowski, S. Menzel, R. Waser, and R. Dittmann, Adv. Mater. **29**, 1700212 (2017).
[14] E. Sediva, W. J. Bowman, J. C. Gonzalez-Rosillo, and J. L. M. Rupp, Adv. Electron. Mater. **5**, 1800566 (2019).
[15] C. Baeumer, C. Schmitz, A. H. H. Ramadan, H. Du, K. Skaja, V. Feyer, P. Muller, B. Arndt, C. L. Jia, J. Mayer, R. A. De Souza, C. Michael Schneider, R. Waser, and R. Dittmann, Nat. Commun. **6**, 8610 (2015).
[16] C. Xu, M. Moors, and R. Dittmann, Appl. Surf. Sci. **359**, 68 (2015).
[17] C. Xu, S. Wicklein, A. Sambri, S. Amoruso, M. Moors, and R. Dittmann, J. Phys. D: Appl. Phys. **47**, 034009 (2014).
[18] F. V. E. Hensling, T. Heisig, N. Raab, C. Baeumer, and R. Dittmann, Solid State Ionics **325**, 247 (2018).
[19] C. Lenser, A. Koehl, I. Slipukhina, H. Du, M. Patt, V. Feyer, C. M. Schneider, M. Lezaic, R. Waser, and R. Dittmann, Adv. Funct. Mater. **25**, 6360 (2015).
[20] J. Xiong, R. Yang, J. Shaibo, H. M. Huang, H. K. He, W. Zhou, and X. Guo, Adv. Funct. Mater. **29**, 1807316 (2019).
[21] F. V. E. Hensling, H. Du, N. Raab, C. L. Jia, J. Mayer, and R. Dittmann, APL Mater. **7**, 101127 (2019).
[22] G. S. Snider, Nanotechnology **18**, 035204 (2007).
[23] K. A. Boahen, *Neuromorphic Systems Engineering* (Springer US, Boston, MA, 2007), pp. 229–259.
[24] R. M. Shelby, G. W. Burr, I. Boybat, and C. Di Nolfo, in *IEEE International Reliability Physics Symposium Proceedings* (IEEE, 2015), p. 6A11.
[25] C. Baeumer, R. Valenta, C. Schmitz, A. Locatelli, T. O. Menteş, S. P. Rogers, A. Sala, N. Raab, S. Nemsak, M. Shim, C. M. Schneider, S. Menzel, R. Waser, and R. Dittmann, ACS Nano **11**, 6921 (2017).
[26] D. J. Keeble, S. Wicklein, L. Jin, C. L. Jia, W. Egger, and R. Dittmann, Phys. Rev. B: Condens. Matter Mater. Phys. **87**, 195409 (2013).
[27] S. Wicklein, A. Sambri, S. Amoruso, X. Wang, R. Bruzzese, A. Koehl, and R. Dittmann, Appl. Phys. Lett. **101**, 131601 (2012).
[28] K. Shibuya, R. Dittmann, S. Mi, and R. Waser, Adv. Mater. **22**, 411 (2010).
[29] M. Kawasaki, K. Takahashi, T. Maeda, R. Tsuchiya, M. Shinohara, O. Ishiyama, T. Yonezawa, M. Yoshimoto, and H. Koinuma, Science **266**, 1540 (1994).
[30] G. Koster, B. L. Kropman, G. J. H. M. Rijnders, D. H. A. Blank, and H. Rogalla, Mater. Sci. Eng., B **56**, 209 (1998).
[31] W. Weibull, J. Appl. Mech. **18**, 293 (1951), https://www.semanticscholar.org/paper/A-Statistical-Distribution-Function-of-Wide-Weibull/88c37770028e7ed61180a34d6a837a9a4db3b264.
[32] R. A. De Souza, V. Metlenko, D. Park, and T. E. Weirich, Phys. Rev. B **85**, 174109 (2012).
[33] D. Marrocchelli, L. Sun, and B. Yildiz, J. Am. Chem. Soc. **137**, 4735 (2015).
[34] Z. Zhang, W. Sigle, R. A. De Souza, W. Kurtz, J. Maier, and M. Rühle, Acta Mater. **53**, 5007 (2005).
[35] T. Heisig, J. Kler, H. Du, C. Baeumer, F. Hensling, M. Glöß, M. Moors, A. Locatelli, T. O. Menteş, F. Genuzio, J. Mayer, R. A. De Souza, and R. Dittmann, Adv. Funct. Mater. **30**, 2004118-1 (2020).
[36] S. Piskunov, E. Heifets, R. I. Eglitis, and G. Borstel, Comput. Mater. Sci. **29**, 165 (2004).
[37] O. Madelung, U. Rössler, and M. Schulz, "Strontium oxide (SrO) crystal structure, lattice parameters, thermal expansion," *II-VI and I-VII Compounds; Semimagnetic Compounds* (Springer-Verlag Berlin Heidelberg, 1999), http://materials.springer.com/lb/docs/sm_lbs_978-3-540-31359-5_237.
[38] Y. Hayakawa, A. Himeno, R. Yasuhara, W. Boullart, E. Vecchio, T. Vandeweyer, T. Witters, D. Crotti, M. Jurczak, S. Fujii, S. Ito, Y. Kawashima, Y. Ikeda, A. Kawahara, K. Kawai, Z. Wei, S. Muraoka, K. Shimakawa, T. Mikawa, and S. Yoneda, in *IEEE Symposium on VLSI Circuits, Digest of Technical Papers* (IEEE, 2015).
[39] G. Niu, P. Calka, M. Auf Der Maur, F. Santoni, S. Guha, M. Fraschke, P. Hamoumou, B. Gautier, E. Perez, C. Walczyk, C. Wenger, A. Di Carlo, L. Alff, and T. Schroeder, Sci. Rep. **6**, 25757 (2016).
[40] V. R. Nallagatla, J. Jo, S. K. Acharya, M. Kim, and C. U. Jung, Sci. Rep. **9**, 1188 (2019).
[41] C. Lenser, M. Patt, S. Menzel, A. Köhl, C. Wiemann, C. M. Schneider, R. Waser, and R. Dittmann, Adv. Funct. Mater. **24**, 4466 (2014).
[42] C. Lenser, A. Kuzmin, J. Purans, A. Kalinko, R. Waser, and R. Dittmann, J. Appl. Phys. **111**, 076101 (2012).
[43] S. Menzel, M. Waters, A. Marchewka, U. Böttger, R. Dittmann, and R. Waser, Adv. Funct. Mater. **21**, 4487 (2011).
[44] S. Cho, C. Yun, S. Tappertzhofen, A. Kursumovic, S. Lee, P. Lu, Q. Jia, M. Fan, J. Jian, H. Wang, S. Hofmann, and J. L. MacManus-Driscoll, Nat. Commun. **7**, 12373 (2016).
[45] M. Buckwell, L. Montesi, S. Hudziak, A. Mehonic, and A. J. Kenyon, Nanoscale **7**, 18030 (2015).
[46] U. Celano, L. Goux, A. Belmonte, K. Opsomer, C. Detavernier, M. Jurczak, and W. Vandervorst, in *IEEE International Reliability Physics Symposium Proceedings* (IEEE, 2015), p. MY111.